JACS Au
AN OPEN ACCESS JOURNAL OF THE AMERICAN CHEMICAL SOCIETY

pubs.acs.org/jacsau

Article

Anion-Induced Interfacial Liquid Layers on $LiCoO_2$ in Salt-in-Water Lithium-Ion Batteries

Hyunjeong Oh, Seung-Jae Shin, Eunjin Choi, Hirona Yamagishi, Toshiaki Ohta, Naoaki Yabuuchi, Hun-Gi Jung, Hyungjun Kim,* and Hye Ryung Byon*

Cite This: *JACS Au* 2023, 3, 1392−1402

Read Online

ACCESS | Metrics & More | Article Recommendations | Supporting Information

ABSTRACT: The incompatibility of lithium intercalation electrodes with water has impeded the development of aqueous Li-ion batteries. The key challenge is protons which are generated by water dissociation and deform the electrode structures through intercalation. Distinct from previous approaches utilizing large amounts of electrolyte salts or artificial solid-protective films, we developed liquid-phase protective layers on $LiCoO_2$ (LCO) using a moderate concentration of 0.5∼3 mol kg^{-1} lithium sulfate. Sulfate ion strengthened the hydrogen-bond network and easily formed ion pairs with Li^+, showing strong kosmotropic and hard base characteristics. Our quantum mechanics/molecular mechanics (QM/MM) simulations revealed that sulfate ion paired with Li^+ helped stabilize the LCO surface and reduced the density of free water in the interface region below the point of zero charge (PZC) potential. In addition, *in situ* electrochemical surface-enhanced infrared absorption spectroscopy (SEIRAS) proved the appearance of inner-sphere sulfate complexes above the PZC potential, serving as the protective layers of LCO. The role of anions in stabilizing LCO was correlated with kosmotropic strength (sulfate > nitrate > perchlorate > bistriflimide ($TFSI^-$)) and explained better galvanostatic cyclability in LCO cells.

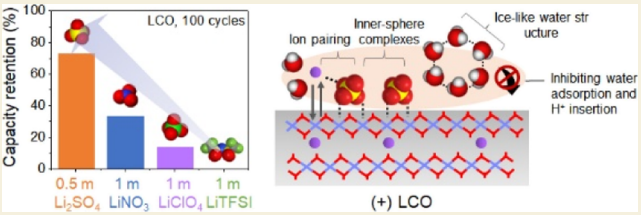

KEYWORDS: *aqueous lithium-ion batteries, in situ electrochemical surface-enhanced infrared absorption spectroscopy, kosmotropic anion, lithium cobalt oxide, QM/MM simulation, sulfate*

Rechargeable aqueous batteries have received much attention as replacements for non-aqueous-based lithium-ion batteries (LIBs) and to utilize future grid-scale energy storage systems (ESSs).[1−3] Aqueous LIBs can improve safety and reduce costs using non-flammable water. In addition, mass production can be implemented promptly by adapting the infrastructure, which has been used for commercialized non-aqueous LIBs. However, they also should overcome the chemical instability of Li-intercalated electrodes in water and the low energy density for practical use. Recent studies have focused on using huge amounts of electrolyte salts, representatively 21 m (molal concentration, mol kg^{-1}) lithium bistriflimide (LiTFSI).[4−7] These electrolytes, called water-in-salt electrolytes (WiSEs), have suppressed the hydrogen evolution reaction (HER) and widened the potential window by forming the aggregated ion pairs and reducing the water activity. By introducing an additional artificial solid-protective layer, the WiSE systems have achieved ∼400 W h kg^{-1} at the cell level.[6,8,9] However, the large quantities of electrolytes in these systems have led to high cost and salt precipitation.[8,10,11]

For economical applications, the use of a moderate concentration of the electrolyte salt, i.e., salt-in-water level, is required. However, one of the big hurdles is the vulnerable Li-intercalated electrodes to water. A water molecule can be easily adsorbed on the bare electrode surface and dissociate into the proton (H^+).[12−16] Subsequently, H^+ diffuses into the electrodes and becomes trapped in the vacancies, which degrades the electrode and impedes Li^+ insertion.[17−21] In the absence of artificial solid-state layers or tremendously concentrated ions (e.g., WiSEs) at the electrode surface, the reversible Li^+ extraction and intercalation processes are highly challenging.

Herein, we introduced a new concept of a liquid-phase anionic protective layer to prevent H^+ insertion. We investigated interfacial reactions of lithium cobalt oxide ($LiCoO_2$, denoted as LCO) with 0.5∼3 m electrolyte salts. A 0.5 m lithium sulfate (Li_2SO_4) solution retarded the electrode degradation in contrast to the 1 m LiTFSI solution that significantly deformed the LCO electrode. It was attributed to the SO_4^{2-} characteristics. SO_4^{2-} strengthened the hydrogen-bond network and was easily paired with Li^+. This strong kosmotropic and hard-base characteristic was compared to nitrate (NO_3^-), perchlorate (ClO_4^-), and $TFSI^-$ as the weaker kosmotropic and soft-based anions. Our mean-

Received: February 8, 2023
Revised: April 17, 2023
Accepted: April 18, 2023
Published: April 28, 2023

https://doi.org/10.1021/jacsau.3c00061
JACS Au 2023, 3, 1392−1402

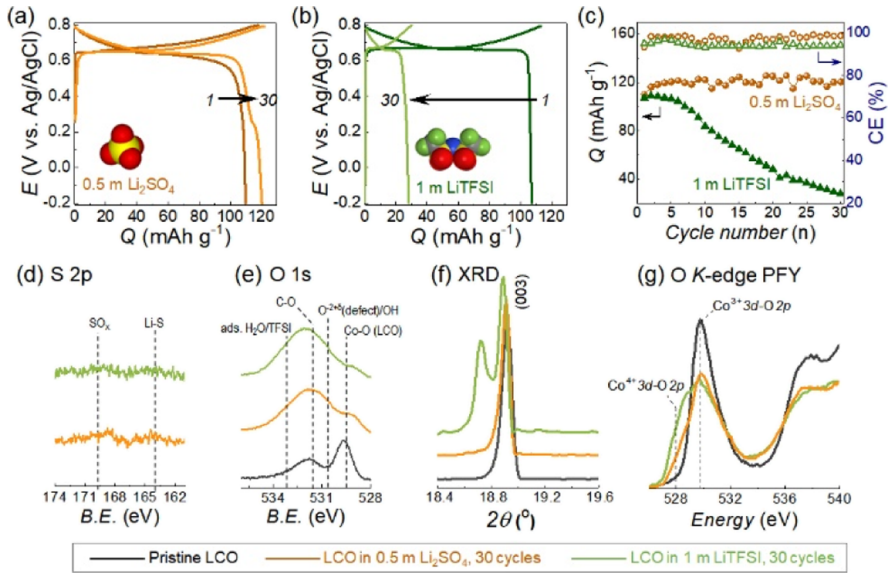

Figure 1. Galvanostatic examinations in LCO half-cells and structural analyses of LCO electrodes with 0.5 m Li_2SO_4 (orange) and 1 m LiTFSI (green). The LCO half-cells comprised LCO, Pt wire, and Ag/AgCl as the working electrode (WE), counter electrode (CE), and reference electrode (RE), respectively. (a−c) Galvanostatic potential profiles of (a) 0.5 m Li_2SO_4 and (b) 1 m LiTFSI for the 1st (dark color) and the 30th cycle (light color) at 0.5 C, and (c) their comparative capacity retention (Q) and Coulombic efficiency (CE). (d,e) XPS of (d) S 2p and (e) O 1s binding energy (B.E.) regions, (f) XRD, and (g) XAFS in the O K-edge region with bulk-sensitive PFY mode for pristine LCO (black) and 30 cycled LCO electrodes with 0.5 m Li_2SO_4 (orange) and 1 m LiTFSI (green).

field Quantum mechanics/molecular mechanics (QM/MM) simulations revealed that SO_4^{2-} tied with Li^+ stayed at the LCO interface below the point of zero charge (PZC) potential, which diminished the density of free water. In addition, *in situ* electrochemical surface-enhanced infrared absorption spectroscopy (SEIRAS) demonstrated the presence of inner-sphere SO_4^{2-} complexes on LCO, serving as the liquid-phase protective layer above the PZC potential. Our study elucidated the superior cyclability of the LCO cells with SO_4^{2-} and better performance with stronger kosmotropic anions.

The motivation of this study was different galvanostatic cyclabilities in two electrolyte solutions, 0.5 m Li_2SO_4 and 1 m LiTFSI in water, where the Li^+ concentrations were constant at 1 m. Galvanostatic tests in half-cells were conducted using LCO on a Ti substrate, Pt coil, and Ag/AgCl as the working electrode (WE), counter electrode (CE), and reference electrode (RE), respectively. There was negligible contamination issue from the Pt CE, confirmed by replacing Pt with an activated carbon (AC) electrode (Figure S1 and Table S1). All examinations were carried out in an argon-purged glovebox to mitigate Co ion diffusion in LCO and stabilize Li^+-intercalation chemistry.[14,22] For 30 cycles, the LCO cells with 0.5 m Li_2SO_4 showed excellent capacity retention with 97% average Coulombic efficiency (CE) (Figure 1a,c). The main plateaus at 0.6−0.8 V (vs Ag/AgCl unless otherwise stated) indicate Li^+ extraction and intercalation during the charge and discharge, respectively, and approached a capacity of 120 mA h g^{-1}. The poor CE for the first cycle (~92%) affected the low average CE (97%) for 30 cycles, which was presumably attributed to the oxygen evolution reaction or water-induced surface activation. We note that the gradual capacity increase was presumably due to improved electrode wettability during cycling.[13] In addition, a minute plateau at 0.25 V often appeared at the end of the discharge, possibly caused by Co^{3+} reduction at the LCO surface. This phenomenon was also observed from non-aqueous electrolyte solutions.[12,23] However, a little Co^{3+} reduction did not significantly disturb 30-times cycled performances (see Figure 1a−c). In sharp contrast, the LCO cells with 1 m LiTFSI exhibited considerable capacity fading from 110 to 30 mA h g^{-1} for 30 cycles and afforded an inferior average CE of 94% (Figure 1b−c).

As expected, there was no cathode electrolyte interphase (CEI), which was a solid-state protective layer arising from the electrolyte decomposition.[24,25] X-ray photoelectron spectra (XPS) exhibited neither SO_4^{2-}- nor $TFSI^-$-related species on the LCO after 30 cycles (Figures 1d and S2). In addition, transmission electron microscopy (TEM) images also revealed no passivation layer on the LCO surface (Figure S3). The bare LCO surface formed defects and surface oxidation by water, as evidenced by the $O^{-2+\delta}$/OH signal at 530.8 eV in XPS (Figure 1e)[21,26] and the partial surface oxidation of the lattice LCO in the oxygen *K*-edge region of surface-sensitive soft X-ray absorption fine structure (XAFS) spectra (partial electron yield mode, <10 nm depth, Figure S4a).[15,27−29] Although the water-induced defects emerged for both LCOs with 0.5 m Li_2SO_4 and 1 m LiTFSI, the latter showed more intense peaks.

In the case of 1 m LiTFSI, the bulk LCO structure was also significantly deformed. The powder X-ray diffraction (XRD) pattern displayed the split 003 reflection of LCO after 30 cycles (Figures 1f and S5). It was attributed to vacant Li^+ sites in LCO and the resulting repulsion of CoO_2 layers that faced each other.[12,15,29,30] Deficient Li^+ was compensated by the Co^{3+} oxidation in LCO. The XAFS spectra in the partial fluorescence yield (PFY) mode (>100 nm depth) validated the pronounced Co^{4+} *3d* ($t_{2g}^5e_g^0$)-O *2p* hybridization band (528 eV), while the original Co^{3+} *3d* hybridization with the O *2p* orbital (529.8 eV) weakened (Figure 1g).[27−29] The blue-shift of the Co^{3+} signal in the Co L_2 and L_3 edge spectra also supported the existence of Co^{4+} (Figure S4b). By contrast, these characteristics were not observed from LCO with 0.5 m Li_2SO_4; no splitting 003 reflection appeared in the XRD pattern, and the XAFS signal corresponding to Co^{4+} *3d*−O *2p*

https://doi.org/10.1021/jacsau.3c00061
JACS Au 2023, 3, 1392−1402

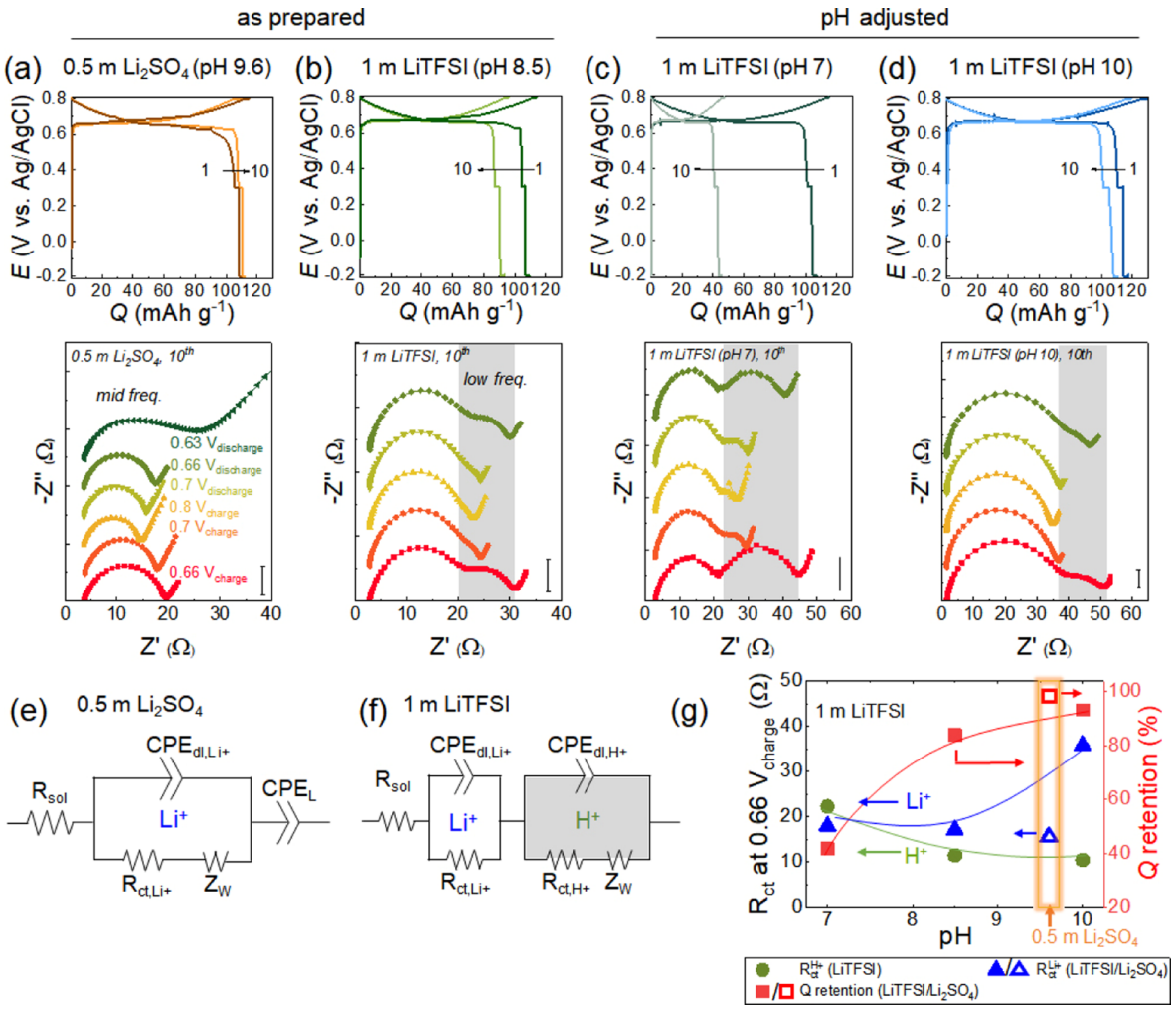

Figure 2. EIS analyses of Li^+ and H^+ extraction and insertion in LCO half-cells during the 10th cycle and correlation between the solution pH and galvanostatic cyclability. (a–d) (Top) galvanostatic profiles of (a) 0.5 m Li_2SO_4 (pH 9.6), (b–d) 1 m LiTFSI at (b) pH 8.5, (c) pH 7, and (d) pH 10 at the 1st (dark color) and the 10th cycle (pale color) at 0.5 C and (bottom) corresponding Nyquist plots during the 10th cycle. The arrows in the galvanostatic curves indicate the directions from the 1st to the 10th cycle. Nyquist plots were acquired after potential holding for 10 min at 0.66 V_{charge} (red), 0.7 V_{charge} (orange), and 0.8 V_{charge} (yellow) and subsequent discharge at 0.7 $V_{discharge}$ (pale green), 0.66 $V_{discharge}$ (green), and 0.63 $V_{discharge}$ (dark green, Li_2SO_4 only). The low-frequency semicircles appearing in 1 m LiTFSI solutions are indicated by the gray box in Nyquist plots, and the *y*-axis scales indicate 5 Ω. (e–f) Equivalent circuits with (e) 0.5 m Li_2SO_4 and (f) 1 m LiTFSI (regardless of pH). (g) pH dependency of Li^+ (blue triangle) and H^+ insertion (green circle)-related resistances and capacity retention after 10 cycles (red square). Resistances were calculated from the Nyquist plot at 0.66 V_{charge} during the 10th cycle and using equivalent circuits in (e–f). The data at pH 9.6 were with 0.5 m Li_2SO_4 (the open symbols, orange guideline), and others (the closed symbols) were with 1 m LiTFSI.

hybridization was weaker (Figure 1f,g). Less structural deformation of the bulk LCO indicated the gentle surface oxidation only, thus providing better reversibility of Li^+ extraction/intercalation processes with 0.5 m Li_2SO_4.

The deficient Li^+ can be originated from the H^+ insertion in LCO.[17−20] Electrochemical impedance spectroscopy (EIS) decouples the Li^+ charge-transfer resistance from the H^+ insertion one.[19] Figure 2a shows galvanostatic profiles at the 1st and 10th cycles with 0.5 m Li_2SO_4 (top panel) and EIS at the open-circuit potential (OCP), galvanostatic charging (0.66−0.8 V_{charge}), and discharging processes (0.8−0.66 (or 0.63) $V_{discharge}$) during the 10th cycle (bottom panel). These Nyquist plots were acquired after potential holding for 10 min (Figure S6). Compared to the sole capacitance characteristic at OCP (Figure S7), a single semicircle appeared in the mid-frequency region by the Li^+ extraction in 0.5 m Li_2SO_4 (Figure S8). The size of the semicircle was reduced during the charging process since the LCO became a semi-metal,[31] whereas it was expanded during the discharging process due to the Li^+ intercalation (Figures 2a and S8a,b). At 0.63 $V_{discharge}$ (dark green), the Li^+ filling in the topmost surface enlarged the semicircles.[32] Therefore, the mid-frequency semicircle was attributed to the Li^+ charge-transfer resistance (R_{ct}^{Li+}, Figure S9a).[19,20,33] This characteristic was repeated over 10 cycles without a notable change in 0.5 m Li_2SO_4 (Figures S8b and 2a), and after 30 cycles, the R_{ct}^{Li+} was estimated as 27.8 Ω based on an equivalent circuit (Figures 2e, S8c, and Table S2).

The LCO electrodes with 1 m LiTFSI (pH 8.5) also showed identical mid-frequency semicircles (Figures 2b and S8d,e). However, a low-frequency semicircle additionally emerged at 0.66 $V_{discharge}$ and disappeared in the following 0.66 V_{charge} (the gray box in the bottom panel of Figures 2b, S8d,e, and S9b). This signal gradually expanded and became irreversible during cycling. After 30 cycles, the R_{ct} for the low-frequency cell was 147 Ω, which was distinct from R_{ct}^{Li+} at 27.6 Ω, appearing at the mid-frequency (Figure S8f and Table S2). We attribute this

https://doi.org/10.1021/jacsau.3c00061
JACS Au 2023, 3, 1392−1402

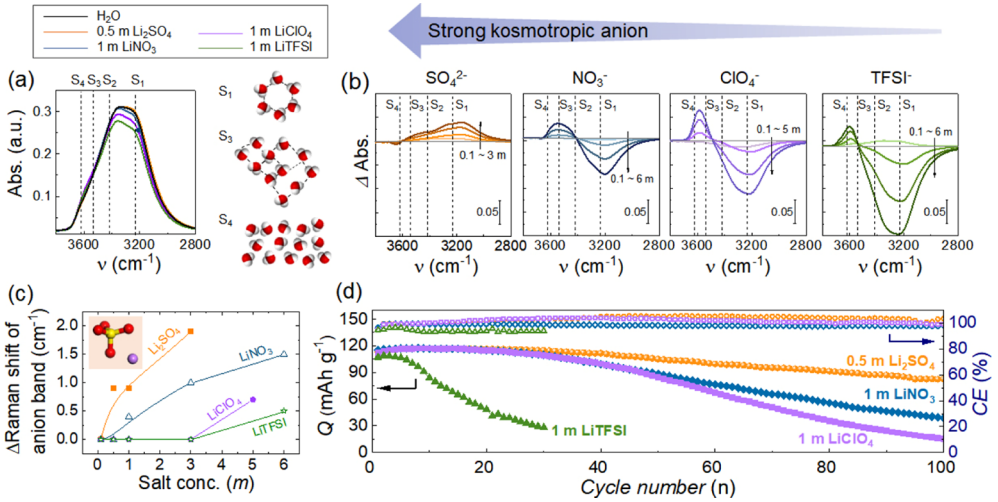

Figure 3. Kosmotropic characters of anions in bulk electrolyte solutions and the correlated galvanostatic cyclability. (a) Comparative ATR-FTIR spectra of pure water (black) and with Li_2SO_4 (orange), $LiNO_3$ (blue), $LiClO_4$ (purple), and LiTFSI (green) electrolytes. The vertically dashed lines indicate O−H stretching bands [ν(O−H)], designated as the ice-like water structure (S_1 and S_2), liquid-like water structure (S_3), and disordered free water molecules (S_4). The right panel schemes represent the corresponding water structures. (b) Difference ATR-FTIR spectra of the ν(O−H) from the pure water (baseline) with increasing salt concentrations. The kosmotropic strength of the anion is indicated on the top. The vertical dashed lines indicate S_1 to S_4 from the right to the left direction. (c) Raman band shifts of anions with increasing electrolyte concentrations. The inset image displays an ion pairing of SO_4^{2-} and Li^+, causing the blueshift of anion vibrations. (d) Comparative cycling profiles of LCO half-cells for 100 cycles with 0.5 m Li_2SO_4, 1 m $LiNO_3$, 1 m $LiClO_4$, and 1 m LiTFSI. The current rate was 0.5 C, and the potential range was −0.2∼0.8 V vs Ag/AgCl.

resistance to the H^+ charge transfer (R_{ct}^{H+}) (Figure 2f),[19,20] and this assignment was validated by its pH dependence; a low-frequency semicircle was larger at pH ∼7 than those at pH 8.5 and 10, and this R_{ct}^{H+} existed irreversibly at pH ∼7 and 8.5 throughout the 10th cycle (Figure 2b−d). Note that a large mid-frequency R_{ct}^{Li+} at pH 10 might be due to the amorphized surface,[34] while a minute H^+ in the electrolyte solution resulted in a small low-frequency R_{ct}^{H+}. The increased low-frequency semicircle below 0.66 $V_{discharge}$ indicated the typical H^+ insertion period to the end of the Li^+ intercalation. Besides, as shown in sequential EIS (Figure S10), the low-frequency semicircle appeared more significantly in the next charging process (0.66 V_{charge}), revealing the continuity of H^+ insertion until the end of discharge (−0.2 $V_{discharge}$). Such an undesired H^+ intercalation affected the cycling performance; LCO cells did not operate reliably at pH < 7, whereas little H^+ insertion at high pH provided better cyclability (top panel in Figure 2b−d).

These results seemingly suggested that different cyclability between 0.5 m Li_2SO_4 and 1 m LiTFSI solutions was attributed to different solution pH. Indeed, the pH of 1 m LiTFSI solution was 8.5, which was lower than that of 0.5 m Li_2SO_4 solution at pH 9.6, measured in the Ar-filled glovebox (Table S1 and Figure S1). However, when similar pH solutions, 0.5 m Li_2SO_4 (pH 9.6) and 1 m LiTFSI (pH 10 by adding LiOH), were compared, the former still showed better cyclability and less H^+ insertion after 10 cycles (Figure 2g). The difference in capacity retention was more significant for elongated cycles. The 0.5 m Li_2SO_4 solution provided insignificant capacity fading after 30 cycles and ∼84% retention after 70 cycles, whereas the 1 m LiTFSI solution at pH 10 retained only ∼34% capacity after 30 cycles (Figure S11), engendering the appearance of R_{ct}^{H+} from the third cycle (Figure S12). Consequently, the pH effect is not the critical factor determining cyclability under mildly alkaline conditions.

Next, we focused on anion characteristics. SO_4^{2-} has a smaller size and a higher charge density than $TFSI^-$. Such a hard-base anion intimately interacts with water and forms a rigid solvation structure, called strong kosmotropic properties according to the Hofmeister series.[35−38] More importantly, the interaction between SO_4^{2-} and water is similar to that between water and water molecules.[45] Thus, SO_4^{2-} does not change the hydrogen-bond network structure but gradually reinforces this bonding strength with increasing concentrations. The strong kosmotropic anion, therefore, serves as a water-structure maker. In contrast, weak kosmotropic anion (i.e., strong chaotropic properties) $TFSI^-$ interacts with water feebly and weakens the overall hydrogen-bond strength of water, which acts as a water-structure breaker. It is noted that the effective range of anions determining the water structures has been debated, from the first solvation shell range to the mid/long-range hydrogen-bonding network.[39−41] Nonetheless, it is generally agreed that the anions profoundly influence the nearby water interactions, and the strength of the anion−water interaction determines the macroscopic solution properties.[40]

To demonstrate a correlation of kosmotropic property to galvanostatic cyclability, we additionally examined NO_3^- and ClO_4^-. Kosmotropic property strengthens in the order of $TFSI^- < ClO_4^- < NO_3^- < SO_4^{2-}$ according to the Hofmeister series. First, the hydrogen-bond strength of the water was observed by the O−H stretching bands [ν(O−H)] in the bulk aqueous electrolyte solutions. Using attenuated total reflection-infrared (ATR-IR) spectrum of pure water, four ν(O−H) bands are assigned to an ice-like ordered structure (S_1, ∼3230 cm^{-1}), ice-like liquid structure (S_2, ∼3420 cm^{-1}), liquid-like amorphous structure (S_3, 3540 cm^{-1}), and disordered water structure where monomeric water molecules are randomly positioned (S_4, ∼3620 cm^{-1}) (Figure 3a).[42−45] In the range of 0.5 ∼ 1 m, ν(O−H) intensities belonging to the ice-like water structures (S_1 and S_2) were attenuated with the weaker kosmotropic anions.[46−49] Furthermore, a change of S_1−S_4

https://doi.org/10.1021/jacsau.3c00061
JACS Au 2023, 3, 1392−1402

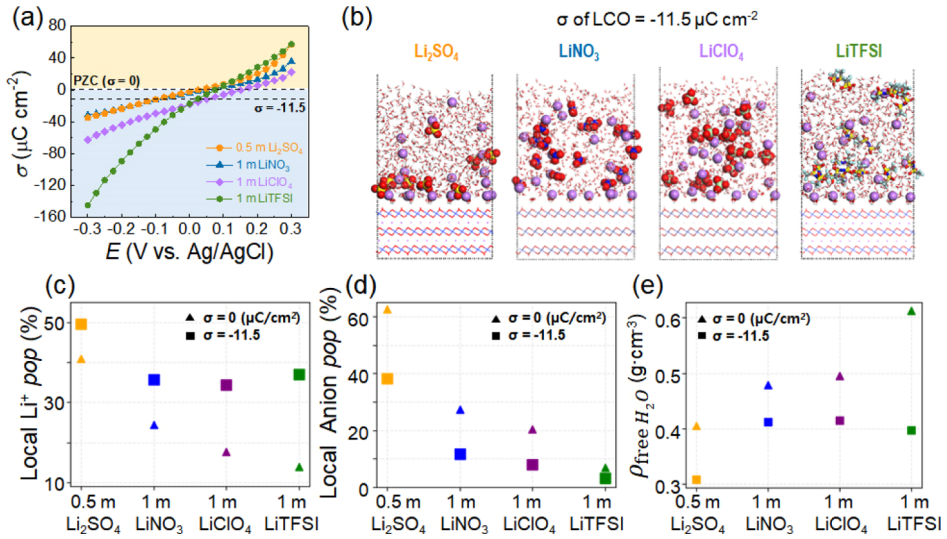

Figure 4. Electric double-layer capacitance (C_{dl}) and mean-field QM/MM simulations of the ion concentrations at the interfacial region. (a) Areal surface charge density (σ) estimated from areal C_{dl} in LCO half-cells. The yellow and blue region indicates the above and below PZC potential, respectively. (b) Representative structural details at $\sigma = -11.5$ μC cm^{-2}. Color codes are; purple for Li^+, red for O, yellow for S, gray for C, cyan for F, blue for N, and light green for Cl. Li^+ and SO_4^{2-} are displayed using spheres, while water and LCO are displayed using sticks. (c–e) Mean-field QM/MM simulation results of (c) local Li^+ population, (d) local anion population (*pop*), and (e) free water density ($\rho_{freeH2O}$) for various electrolyte salts in the interfacial region.

signals was profound with increasing electrolyte concentrations. From the pure water spectrum as a baseline, the deviation of the ν(O–H) band appeared in Figures 3b and S13. The S_1 and S_2 bands were enhanced with the increased Li_2SO_4 concentration, verifying the strengthened hydrogen bond. In sharp contrast, the intensities of S_1 and S_2 declined with increasing $LiNO_3$, $LiClO_4$, and LiTFSI amounts,[45] while the disorderness of the water structures (S_3 and S_4 bands) was intense, assuming that the Li^+ effect was constant for all samples. This trend was more significant with the weaker kosmotropic property, validating the role of a water-structure breaker. Similar behaviors were also observed from the Raman spectra (Figure S14).

Along with the anion–water interaction, the ion–ion interaction should also be considered. The hard-base anion (i.e., strong kosmotropic anion) favorably forms an ion pair with the hard-acid Li^+ according to the hard and soft acid and base (HSAB) concept.[50,51] The appearance of an IR-inactive stretching band and the red-shift of the anti-symmetric SO_4^{2-} vibration evidenced the growing number of ion associations (Figure S15).[48] Blue-shifting anion bands in the Raman spectrum also signified the formation of ion pairs and showed dependency on the kosmotropic strength; Li_2SO_4 exhibited the apparent blue-shift even at 0.5 m, and the shift was more significant with increasing concentrations, whereas there was no shift with $LiClO_4$ and LiTFSI below 3 m (Figures 3c and S16).[6,7,43,51−53] Taken together, strong kosmotropic anions retained the ice-like water structure through the strong hydrogen-bond network and also tended to form ion pairs with Li^+ ions.

Notably, such a kosmotropic propensity was correlated with galvanostatic cell performances. The 0.5 m Li_2SO_4 solution exhibited 73% capacity retention after 100 cycles (Figures 3d and S17). In comparison, 1 m $LiNO_3$ (pH 9.2) and 1 m $LiClO_4$ (pH 8.9) provided 33 and 13% capacity retention, respectively (Figures S11 and S17). These cyclability results corresponded to a smaller R_{ct}^{H+} with 1 m $LiNO_3$ than that with $LiClO_4$ (Figure S18). The 1 m LiTFSI solution underwent a rapid capacity drop during the initial 30 cycles. The CE was ∼94% with 1 m LiTFSI solution, which was the lowest among those obtained with the other solutions. Thus, stronger kosmotropic anions in the LCO cells showed better cyclability, suggesting that the ice-like water structure and favorable ion association stabilized the LCO.

Interestingly, when the discharging cut-off potential shifted from −0.2 $V_{discharge}$ to 0.3 $V_{discharge}$, the cyclability was ameliorated for all electrolyte salts. The capacity retention ranged from <35 to 56% with 1 m $LiNO_3$, 65% with 1 m $LiClO_4$, and 21% with 1 m LiTFSI over 200 cycles, and the cells with 0.5 m Li_2SO_4 still exhibited superior performance (67%) (Figures S19 and S20 and Table S3). It indicated the significant capacity loss at 0.3∼−0.2 $V_{discharge}$ as H^+ was inserted.

To elucidate the different degrees of the H^+ insertion, the anion and water interactions at the LCO/electrolyte solution interface were investigated. We measured the electric double-layer (EDL) capacitance (C_{dl}) by the staircase-potential EIS in this non-faradaic potential region (Figures S21 and S22) and estimated the surface charge density (σ) of LCO (eq 1)

$$\sigma = \int_{UPZC}^{U} C_{dl}(U')\mathrm{d}U' \tag{1}$$

where U is the electrode potential and U^{PZC} is the PZC potential at the minimum C_{dl}. The surface charge density–potential curves in Figure 4a indicate the U^{PZC} ($\sigma = 0$) at 0 V in 0.5 m Li_2SO_4, 0.07 V in 1 m $LiNO_3$ and LiTFSI, and 0.15 V in 1 m $LiClO_4$ solution. Apparently, the LCO surfaces are negatively charged below 0 V for all electrolyte cases, where Li^+ and H^+ are attracted to LCO, while the anions are repelled through electrostatic interactions.

Comparing the C_{dl}, the LCO with 1 m LiTFSI had 1.5–3 times higher value than that with the other electrolytes, as shown in staircase EIS and cyclic voltammogram (Figures S22 and S23), which should be addressed first. Above the U^{PZC}, the

https://doi.org/10.1021/jacsau.3c00061
JACS Au 2023, 3, 1392−1402

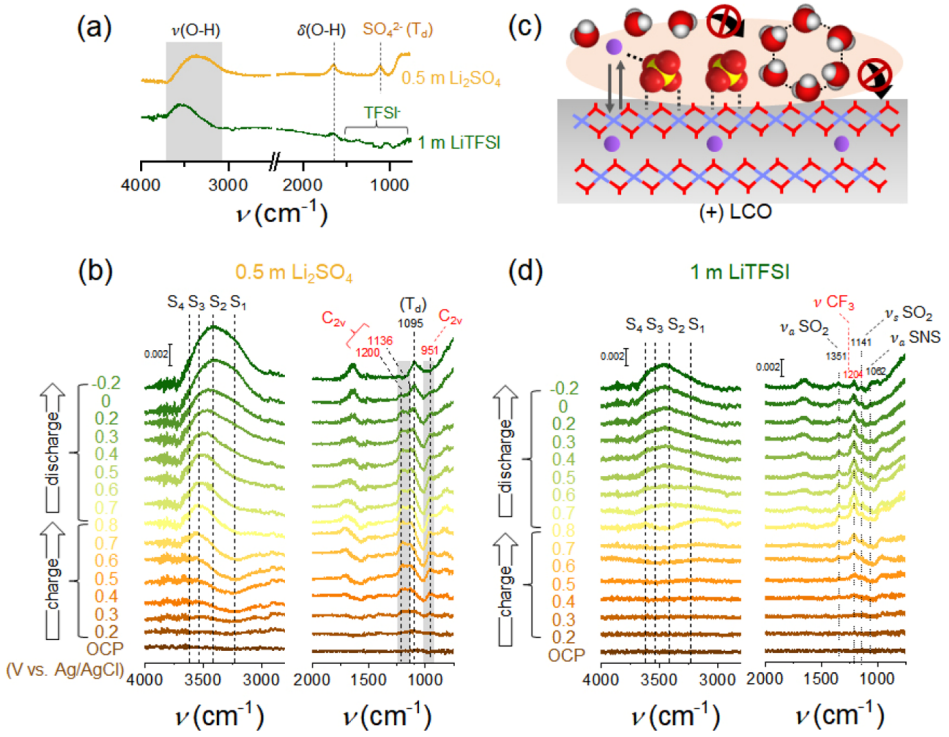

Figure 5. *In situ* electrochemical SEIRAS analyses of LCO electrodes with 0.5 m Li_2SO_4 and 1 m LiTFSI during the second cycle. The LCO film (∼100 nm of thickness) was deposited on Au/ZnSe, and CE and RE were Pt wire and Ag/AgCl, respectively. (a) SEIRAS spectra of LCO with 0.5 m Li_2SO_4 (orange, top) and 1 m LiTFSI (dark green bottom) at OCP after the first cycle, showing ν(O−H), H_2O bending mode [δ(H−O−H)], and anion vibration. (b, d) Difference SEIRAS spectra during the potential sweep from 0.2 V_{charge} to 0.8 V_{charge}, followed by 0.8 $V_{discharge}$ to −0.2 $V_{discharge}$. The baseline was obtained from OCP, and other potential-dependent spectra deviated from OCP. The IR spectra were collected during 3 min potential holding. The dashed lines of S_1−S_4 indicate ν(O−H) corresponding to the water structures. The anion bands are assigned below 1500 cm^{-1}. (c) Schematic illustration of liquid-phase protective layers comprising inner-sphere SO_4^{2-} complexes, Li^+ (purple), and water.

higher C_{dl} is explained by the higher $TFSI^-$ population in the EDL because of the large van der Waals (vdW) volume, high polarizability, and mild hydrophilicity of $TFSI^-$.[54−56] Below the U^{PZC}, where the polarity of the electrode charge is reversed, the Li^+ ions are accumulated on the LCO surface. Ion pairing is an important phenomenon in determining the C_{dl} value. Because $TFSI^-$ ions have a low association with the accumulated Li^+ ions through the HSAB concept, the population of anions is lowered, and the amount of net ionic charge from Li^+ ions is maximized, enabling the highest C_{dl} (Figure S22). Conversely, stronger kosmotropic anions than $TFSI^-$ tend to favorably pair with Li^+ below the U^{PZC} and nullify the net ionic charge, explaining the lower C_{dl}.

Our recently developed mean-field QM/MM simulation (Figures S24 and S25 and 4b)[57] provides atom-resolved information about ion and water distributions at the interfacial and EDL regions. We particularly compare two different surface charge densities of $\sigma = 0$ (at U^{PZC}) and −11.5 $\mu C\ cm^{-2}$ (below the U^{PZC}) since the negatively charged LCO, where the anions depleted and the electrode tended to be exposed to the water, yields a significant H^+ insertion and a capacity fading, as shown in Figure S8 and Table S3. The local ion and water density profiles show a layering tendency near the electrode surface and converge to the bulk value at $z > \sim 6$ Å (Figure S24). Thus, we analyzed the region at $z < 6$ Å to understand the structure of the EDL in direct contact with the solid electrode.

At the PZC ($\sigma = 0$), stronger kosmotropic anions are concentrated in the interfacial region (Figure S24). When the LCO is negatively charged with $\sigma = -11.5\ \mu C\ cm^{-2}$, Li^+ ions are attracted to the LCO surface due to the electrostatic interaction (Figure 4c). Interestingly, although the anions experience electrostatic repulsion from the negatively polarized electrode, the local anion concentration is still maintained to be high for SO_4^{2-} compared to other anions (Figure 4d). This is attributed to the high local concentration of Li^+, which forms a contact ion pair (CIP) with the strong kosmotropic anion (Figure S26). Thus, the local ion concentration in the EDL becomes the largest for the Li_2SO_4, maximizing the number of ion-coordinating water species in the interfacial region (Figure 4e), which stabilizes the interfacial water. Thus, the density of free water, which is not coordinated by the ion and thereby is preferable to form either water−water or water-LCO interactions,[7] is reduced (Figure 4e). It reasons that the Li_2SO_4 electrolyte solution stabilizes LCO below the U^{PZC}. In contrast, the weak kosmotropic anion has a negligible association with Li^+. Besides, the electrostatic repulsion among Li^+ ions lowers the local Li^+ population and increases the free-water density (Figure 4c−e). Therefore, the kosmotropic strength is inversely related to the density of free water below the U^{PZC}, which accounts for better cyclability using the stronger kosmotropic anion.

Experimentally, the interfacial region was observed by *in situ* electrochemical SEIRAS.[58] The LCO film (∼100 nm thick including 10−15 nm size of nanoparticles, Figure S27) was deposited on a gold-coated ZnSe prism using ion sputtering. At the OCP, the SEIRAS graph of 0.5 m Li_2SO_4 solution exhibited similar characteristics of the bulk electrolyte (Figure 5a); the ν(O−H) and H_2O bending mode [δ(H−O−H)] appeared at 3200−3620 cm^{-1} and 1648 cm^{-1}, respectively, and

https://doi.org/10.1021/jacsau.3c00061
JACS Au 2023, 3, 1392−1402

the tetrahedral (T_d) geometry of SO_4^{2-} band emerged at 1110 cm^{-1}. Using this spectrum as a baseline, the deviation of the spectrum was collected through potential steps and holding the desired potential for 3 min (Figure 5b). During the charging process from 0.6 V_{charge}, the S_3 of the ν(O−H) band intensified, reflecting the existing partially disordered water structure. Below 0 $V_{discharge}$, *i.e.,* below the U^{PZC}, the S_1 and S_2 bands were pronounced as the bulk water structure with Li_2SO_4 was recovered. A similar tendency was also observed on the LCO-free gold film on Si prism (Figure S28), suggesting that these water behaviors were associated with the ion-charging process at the interface.

More importantly, the T_d geometry of the SO_4^{2-} was transformed to the C_{2v} point group at the LCO surface during the charging and discharging processes. At 0.4 V_{charge}−0.3 $V_{discharge}$, the C_{2v} geometry vibrations newly appeared at 951, 1136, and 1200 cm^{-1} (Figure 5b). LCO (the central Co ion) was coordinated by the bidentate SO_4^{2-} ligand, forming the inner-sphere SO_4^{2-} surface complexes (Figure 5c).[59,60] These C_{2v} bands of SO_4^{2-} were attenuated below 0 $V_{discharge}$, while the T_d band of SO_4^{2-} re-appeared with the increased S_1 and S_2 bands, verifying the disappearance of the inner-sphere SO_4^{2-} protective layer below the U^{PZC}. Thus, the SO_4^{2-} adlayer can protect the LCO above the U^{PZC} and improve the LCO stability.

In comparison, the LCO with 1 m LiTFSI was also observed from the OCP, showing the bulk electrolyte solution characteristics (Figure 5a). The CF_3 stretching band of $TFSI^-$ at 1204 cm^{-1} was intensified during the charging process and remained for the discharging process (Figure 5d).[58] Below 0 $V_{discharge}$, the CF_3 stretching band was attenuated as the LCO surface was negatively electrified. Although this behavior was similar to the one with Li_2SO_4 solution, there was no evidence for forming inner-sphere $TFSI^-$ complexes. The absence of the protective layer also caused poor cell cyclability (Figure 3d).

In all, the key concept of the protective layer is the inner-sphere SO_4^{2-} complexes above the U^{PZC}. In addition, detached SO_4^{2-} below the U^{PZC} forms the ion pairs close to the LCO surface, lowering the density of free water and suppressing the H^+ insertion. Using $LiNO_3$, $LiClO_4$, and LiTFSI, the ability of the protective layer was examined by extending the electrochemical potential window. Positive potential windows were widened with increasing electrolyte concentrations (0.5∼6 m) on Ti electrodes (Figure 6a and Figure S29) because the amount of free water was reduced at the interface. In addition, the positive-potential window was extended with stronger kosmotropic anions; 3 m Li_2SO_4 exhibited the widest expansion among the 3 m of the all electrolytes and even better than 5−6 m of the weaker kosmotropic ones (Figure 6b,c). Thus, we anticipate stronger anion interaction with the LCO surface, in particular for the effective inner-sphere SO_4^{2-} complex layer. In comparison, the negative-potential range (<−0.2 V, far away from the U^{PZC}) was not considerably elongated on the LCO (Figure S29). In this condition, the water molecules approach the electrode surface intensely, and the EDL structure at the LCO/electrolyte solution is changed.

The full-cell performances of aqueous cells were then examined using $Li_{9/7-x}Nb_{2/7}Mo_{3/7}O_2$ (LNMO) negative electrodes[61,62] and LCO positive electrodes. LNMO showed poor performances in the 0.5∼1 m electrolyte solutions due to the severe HER (Figure S30a,b), reasoning the rapid capacity fading in the full cells (Figure 6d). In comparison, LNMO

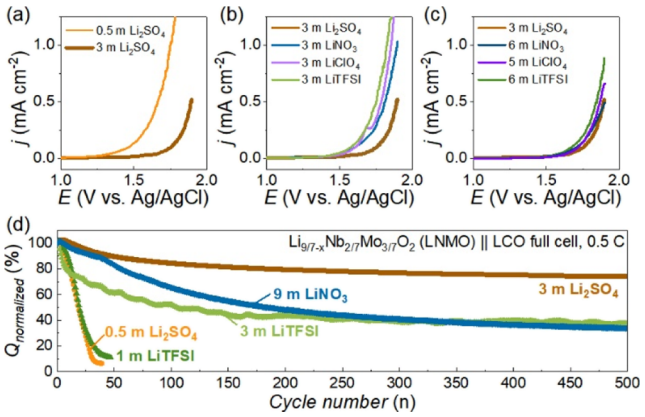

Figure 6. Positive potential windows with different electrolyte concentrations and galvanostatic cyclability in full cells. (a−c) Comparative electrochemical potential windows toward positive potential on Ti (WE) with (a) 0.5 and 3 m Li_2SO_4, (b) 3 m electrolytes, and (c) 6 m $LiNO_3$, 5 m $LiClO_4$, and 6 m LiTFSI compared to 3 m Li_2SO_4. All scan rates were 0.2 mV s^{-1}. (d) Capacity retention and CE in $Li_{9/7-x}Nb_{2/7}Mo_{3/7}O_2$ (LNMO) ||LCO full cells at 0.5 C for a total of 500 cycles.

exhibited better capacity retention at 3 m of the electrolyte concentration (Figure S30c−e). The 3 m Li_2SO_4 delivered 74% capacity retention in full cells over 500 cycles, which was superior to that achieved with 3 m LiTFSI (38%) and 9 m $LiNO_3$ (34%) (Figures 6d, S31,32, and Table S4). Under the assumption that all LNMO electrodes were comparably stable, the outstanding cyclability of 3 m Li_2SO_4 was attributed to the LCO stability. Therefore, SO_4^{2-} succeeded in protecting the LCO surface in the full cells and demonstrated the effect of strong kosmotropic anion in the aqueous electrolyte solutions.

In summary, we demonstrated the imperative role of anions in retarding electrode deformation with salt-in-water electrolytes. Sulfate ion mitigated H^+ insertion into LCO, providing a capacity fading rate of 0.20% per cycle over 200 cycles with 0.5 m Li_2SO_4 in half-cells and 0.06% fading rate per cycle with 3 m Li_2SO_4 for 500 cycles in full cells. At the interface, the sulfate ions formed inner-sphere surface complexes and depleted the water adsorption sites during the charging and discharging processes. In addition, sulfate ions induced water molecules to form strong hydrogen bonds. Atomic-scale multiscale simulations illuminated the strong association of Li^+ with sulfate ions, which reduced the density of free water on the electrode at the end of discharge. Thus, the performance of sulfate ions was excellent in stabilizing LCO. In contrast, nitrate, perchlorate, and $TFSI^-$ accelerated capacity fading, underpinning the critical anion characteristics. This fundamental understanding sheds light on dynamic interfacial structures and the associated LCO stability in aqueous LIBs.

METHODS

Chemicals

For electrolyte, $LiN(SO_2CF_3)_2$ [lithium bis(trifluoromethanesulfonyl) imide, LiTFSI, >99.7%, Kanto], $HN(SO_2CF_3)_2$ [bis tri-(fuloromethanesulfonly) imide, HTFSI, >99.0%, TCI], Li_2SO_4 (99.7% Alfa aesar), $LiNO_3$ (reagent plus, Sigma-Aldrich), $LiClO_4$, (99.99%, Sigma-Aldrich), and LiOH (>98%, Sigma-Aldrich) were used as received without any purification. For electrodes, $LiCoO_2$ (99.8%), *N*-methylpyrrolidine (NMP), and H_2O_2 (30% in H_2O) were purchased from Sigma-Aldrich, and NH_4OH was purchased from Fluka (5.0 M).

https://doi.org/10.1021/jacsau.3c00061
JACS Au 2023, 3, 1392−1402

Preparation of Electrodes

$LiCoO_2$ (LCO) powders were mixed with Super P carbon (Timcal) and polyvinyldene fluoride (PVDF, Kynar) binder with 8/1/1 wt %, respectively, with NMP and blended using a planetary mixer (Thinky, ARE-310). This slurry was cast on the titanium (Ti) foil (Wellcos, 99.5% thickness (t) = 20 μm) or carbon paper (Toray, TGP-H-120) using the doctor blade method, followed by drying at 80 °C overnight in the thermal oven. The weight of the active material was 2.5∼5 mg cm^{-2}. The active carbon (AC) electrode was also prepared by the same method with 9/1 wt % of AC and PVDF binder. The Ti foil was pre-treated using the piranha solution (7/3 v/v of NH_4OH/H_2O_2, respectively).

A Li-excess Mo-based cation-disordered rock salt oxide, $Li_{9/7-x}Nb_{2/7}Mo_{3/7}O_2$ (LNMO), was prepared according to the previous report.[61] The LNMO was cast on the carbon paper with 4∼8 mg cm^{-2} of mass loading. This negative electrode was completed by soaking in H_2O with stirring for 2 h for Li^+ extraction.[62]

Electrochemical Measurements

All electrochemical tests were conducted in an argon (Ar)-filled glovebox. Half-cell tests were examined through cyclic voltammetry and galvanostatic cycles. The three-electrode cells were composed of the WE of LCO on the Ti foil [diameter (d) = 6 mm], the CE of platinum (Pt) coil, and the RE of Ag/AgCl (3 M NaCl). All tests were conducted using an electrochemical tester (VMP-3, Biologic). The de-gassing process was achieved through Ar gas purging in the glovebox before tests.[22]

Full cells were prepared using 2032-type coin cells, and galvanostatic electrochemical examinations were examined using a battery cycler (PNE, PESC05-0.1). The LCO electrode on the carbon paper (d = 12 mm) was assembled with the delithiated LNMO (d = 14 mm) on the carbon and a piece of GF/C separator (d = 19 mm, Whatman) in an Ar-filled glovebox. The weight ratio of active materials for LNMO/LCO was 1.5∼2.

EIS tests were carried out with an amplitude of 10 mA and a frequency range of 100 kHz∼0.1 Hz by using an electrochemical tester (VMP-3, Biologic). The EIS for the LCO electrode in the half-cell was measured after holding a programmed potential for 10 min. To measure the electrochemical double-layer capacitance (C_{dl}), staircase-potential EIS was conducted for a potential range of 0.3 to −0.3 V vs Ag/AgCl.[63,64] Every potential step of −25 mV was moved, and EIS was measured after holding a programmed potential for 30 min. All EIS data were fit using EC-lab software based on reasonable equivalent circuit models.

In situ ATR-SEIRAS (iS50, Thermo Scientific) tests were conducted with ZnSe prisms (incident angle: 54°, PIKE Technologies) or Si prisms and MCT/B detector (HgCdTe, PIKE Technologies). A gold film was first deposited on a ZnSe prism using an ion sputter (Korea vacuum tech, Intelsi-S Bench-Top sputter coater) to form ∼50 nm thickness. Afterward, LCO was deposited using the RF magnetron sputtering system (KVS-T4060, Daedong high technologies) to be a thickness of 100 nm. Scanning electron microscopy (Magellan400, FEI Co) at the KAIST Analysis Center for Research Advancement (KARA) and atomic force microscopy (AFM, Agilent 5500 SPM) were used for surface morphology observations of LCO on gold films. The complete LCO/gold/ZnSe prism was used for WE. Pt coil and Ag/AgCl (sat. KCl) were used for CE and RE, respectively. Spectra were measured during a staircase-potential sweep from OCP to 0.8 V, followed by 0.8 to −0.2 V vs Ag/AgCl with a 0.1 V potential step. The constant potential was held for 3 min at each potential step to measure the IR spectrum. The IR spectrum at OCP was used as the baseline. We noted that sputtered LCO had an amorphous structure and was not fully involved in the Li^+ extraction and intercalation processes. Crystallization of LCO by annealing in air at 550 °C for 5 h made ZnSe prism to ZnO that was not transparent in the given wavenumber range. Nonetheless, this study was valuable for observing anion interaction at the LCO surfaces and gave insights into the interfacial structures.

Characterizations

The pH of electrolyte solutions was measured using a pH meter (Mettler Toledo pH/Ion meter) after sufficient Ar-gas purging in an Ar-filled glovebox and removed from the glovebox. It was noted that pH was constant in the Ar-filled glovebox for several days, while the pH decreased after air exposure. For post-mortem analyses, LCO electrodes were washed with de-gassed distilled (DI) water and dried under a vacuum at 60 °C overnight. Soft X-ray absorption near-edge structure (XANES) was measured in the BL11, Synchrotron Radiation (SR) center at Ritsumeikan University. The LCO electrodes were not exposed to air and directly transferred to the XANES chamber using a hermetic vessel. XRD (Cu Kα, Rigaku) was used to analyze the long-range order of the crystal structure. XPS (Al Kα, Thermo VG Scientific) was used for surface analysis. All spectra were calibrated to the carbon 1s sp^2 hybridization signal at 248.5 eV. TEM (FEI Tecnai GE F30 S-Twin (300 kV)) images were attained to observe the surface layer. All XRD, XPS, and TEM were used at KARA. The OH stretching vibrations of aqueous electrolyte solutions were attained from ATR-IR spectroscopy in the range of 400∼4000 cm^{-1} (iS50, diamond window, Thermo Scientific). Confocal Raman spectroscopy (Andor, SR-750-A-R) was used with a laser of 532 nm wavelength to acquire Raman spectra.

Mean-Field QM/MM Simulations

Mean-field QM/MM simulations were performed using the density functional theory in classical Explicit Solvents (DFT-CES)[57] method. DFT-CES is implemented by combining the Quantum ESPRESSO[65] DFT module and the large-scale atomic/molecular massively parallel simulator (LAMMPS) molecular dynamics (MD) module.[66] The detailed simulation procedure of the DFT-CES can be found in our previous publications.[57,67−69]

The LCO electrode was modeled as the (003) $LiCoO_2$ surface of R $\bar{3}$ m space group at a QM level. Half of the outermost CoO_2 layer was terminated with hydrogen to block overestimating surface property,[70] resulting in a stoichiometry of $Li_{0.66}CoO_2H_{0.33}$. The projector-augmented-wave[71] method was used with the kinetic energy cutoff of 60 Ry and the exchange−correlation using the Perdew−Burke−Ernzerhof functional under the generalized gradient approximation (GGA) scheme.[72] The strongly localized 3d orbital of Co was simulated using the GGA + U method with U_{eff} value to be 4.91 eV.[73] Gaussian smearing was used with a value of 0.02 Ry. The dipole correction along the z-direction was applied to block the unphysical interaction between the images of the cells. The Brillouin zone was sampled by Γ-centered k points of 5 × 5 × 1.

The electrolyte phases of 0.5 m Li_2SO_4 and 1 m LiTFSI, $LiNO_3$, and $LiClO_4$ were modeled using classical force-fields (FFs). 800 numbers of TIP3P[74] water molecules were included along with eight pairs of Li_2SO_4 or 16 pairs of LiTFSI, $LiNO_3$, and $LiClO_4$, respectively. Ions were described using the previously developed FFs,[75−79] and the vdW parameter of the LCO was described using the universal FF.[80] Off-diagonal vdW interactions were modeled using the Lorentz-Bertelot mixing rule. We performed canonical ensemble MD simulations at 300 K using the Nosé-Hoover thermostat.[81,82]

To negatively charge the electrode−electrolyte interface, electrons were inserted into the LCO electrode using DFT, while Li^+ were inserted in the electrolyte phase keeping the total charge of the DFT-CES cell to zero.

■ ASSOCIATED CONTENT

Supporting Information

The Supporting Information is available free of charge at https://pubs.acs.org/doi/10.1021/jacsau.3c00061.

Method, electrochemical and chemical analyses, and details of computational data (PDF)

https://doi.org/10.1021/jacsau.3c00061
JACS Au 2023, 3, 1392−1402

AUTHOR INFORMATION

Corresponding Authors

Hyungjun Kim − *Department of Chemistry, Korea Advanced Institute of Science and Technology (KAIST), Daejeon 34141, Republic of Korea;* orcid.org/0000-0001-8261-9381; Email: linus16@kaist.ac.kr

Hye Ryung Byon − *Department of Chemistry, Korea Advanced Institute of Science and Technology (KAIST), Daejeon 34141, Republic of Korea; Advanced Battery Center, KAIST Institute for NanoCentury, Daejeon 34141, Republic of Korea;* orcid.org/0000-0003-3692-6713; Email: hrbyon@kaist.ac.kr

Authors

Hyunjeong Oh − *Department of Chemistry, Korea Advanced Institute of Science and Technology (KAIST), Daejeon 34141, Republic of Korea; Advanced Battery Center, KAIST Institute for NanoCentury, Daejeon 34141, Republic of Korea*

Seung-Jae Shin − *Department of Chemistry, Korea Advanced Institute of Science and Technology (KAIST), Daejeon 34141, Republic of Korea*

Eunjin Choi − *Department of Chemistry, Korea Advanced Institute of Science and Technology (KAIST), Daejeon 34141, Republic of Korea; Advanced Battery Center, KAIST Institute for NanoCentury, Daejeon 34141, Republic of Korea*

Hirona Yamagishi − *Sychrotron Radiation (SR) Center, Ritsumeikan University, Kusatsu, Shiga 525-8577, Japan*

Toshiaki Ohta − *Sychrotron Radiation (SR) Center, Ritsumeikan University, Kusatsu, Shiga 525-8577, Japan*

Naoaki Yabuuchi − *Department of Chemistry and Life Science, Yokohama National University, Yokohama, Kanagawa 240-8501, Japan;* orcid.org/0000-0002-9404-5693

Hun-Gi Jung − *Energy Storage Research Center, Clean Energy Research Division, Korea Institute of Science and Technology (KIST), Seoul 02792, Republic of Korea;* orcid.org/0000-0002-2162-2680

Complete contact information is available at: https://pubs.acs.org/10.1021/jacsau.3c00061

Author Contributions

H.O. and S.-J.S. contributed equally. H.O. and H.R.B. designed the experiments, and S.-J.S. and H.K designed QM/MM simulations. H.O. and E.C. examined all electrochemical tests and analyses. H.Y. and T.O. analyzed XANES. N.Y. provided LNMO, and H.-G.J. provided the LCO film on Au/ZnSe. H.O., S.-J.S., H.K., and H.R.B. wrote the manuscript, and all authors have given approval to the final version of the manuscript.

Notes

The authors declare no competing financial interest.

ACKNOWLEDGMENTS

This work was supported by the Korea Toray Science Foundation, the KAIST Global Singularity Research Program for 2021, and a National Research Foundation of Korea (NRF) grant funded by the Korean government (MSIT) (nos. NRF2017R1A5A1015365 and 2021R1A5A1030054). Soft XAS experiments were performed with the approval of the program committee (nos. S17024, S18003, and S18030) at the Ritsumeikan University. The authors thank Joo Man Woo for LCO deposition on Au/ZnSe and Minyoung Shim for AFM measurements.

REFERENCES

(1) Alias, N.; Mohamad, A. A. Advances of aqueous rechargeable lithium-ion battery: A review. *J. Power Sources* **2015**, *274*, 237−251.

(2) Wang, Y. G.; Yi, J.; Xia, Y. Y. Recent Progress in Aqueous Lithium-Ion Batteries. *Adv. Energy Mater.* **2012**, *2*, 830−840.

(3) Eftekhari, A. High-Energy Aqueous Lithium Batteries. *Adv. Energy Mater.* **2018**, *8*, 1801156.

(4) McEldrew, M.; Goodwin, Z. A. H.; Kornyshev, A. A.; Bazant, M. Z. Theory of the double layer in water-in-salt electrolytes. *J. Phys. Chem. Lett.* **2018**, *9*, 5840−5846.

(5) Vatamanu, J.; Borodin, O. Ramifications of Water-in-Salt Interfacial Structure at Charged Electrodes for Electrolyte Electrochemical Stability. *J. Phys. Chem. Lett.* **2017**, *8*, 4362−4367.

(6) Suo, L. M.; Oh, D.; Lin, Y. X.; Zhuo, Z. Q.; Borodin, O.; Gao, T.; Wang, F.; Kushima, A.; Wang, Z. Q.; Kim, H. C.; et al. How Solid-Electrolyte Interphase Forms in Aqueous Electrolytes. *J. Am. Chem. Soc.* **2017**, *139*, 18670−18680.

(7) Suo, L. M.; Borodin, O.; Gao, T.; Olguin, M.; Ho, J.; Fan, X. L.; Luo, C.; Wang, C. S.; Xu, K. "Water-in-salt" electrolyte enables high-voltage aqueous lithium-ion chemistries. *Science* **2015**, *350*, 938−943.

(8) Yamada, Y.; Usui, K.; Sodeyama, K.; Ko, S.; Tateyama, Y.; Yamada, A. Hydrate-melt electrolytes for high-energy-density aqueous batteries. *Nat. Energy* **2016**, *1*, 16129.

(9) Yang, C. Y.; Chen, J.; Ji, X.; Pollard, T. P.; Lu, X. J.; Sun, C. J.; Hou, S.; Liu, Q.; Liu, C. M.; Qing, T. T.; et al. Aqueous Li-ion battery enabled by halogen conversion-intercalation chemistry in graphite. *Nature* **2019**, *569*, 245−250.

(10) Wang, J.; Yamada, Y.; Sodeyama, K.; Watanabe, E.; Takada, K.; Tateyama, Y.; Yamada, A. Fire-extinguishing organic electrolytes for safe batteries. *Nat. Energy* **2017**, *3*, 22−29.

(11) Reber, D.; Kuhnel, R. S.; Battaglia, C. Suppressing crystallization of water-in-salt electrolytes by asymmetric anions enables low-temperature operation of high-voltage aqueous batteries. *ACS Mater. Lett.* **2019**, *1*, 44−51.

(12) Ramanujapuram, A.; Gordon, D.; Magasinski, A.; Ward, B.; Nitta, N.; Huang, C.; Yushin, G. Degradation and stabilization of lithium cobalt oxide in aqueous electrolytes. *Energy Environ. Sci.* **2016**, *9*, 1841−1848.

(13) Kobayashi, S.; Nishio, K.; Wilde, M.; Fukutani, K.; Shimizu, R.; Hitosugi, T. Protons inside the LiCoO2 electrode largely increase electrolyte-electrode interface resistance in all-solid-state Li batteries. *J. Phys. Chem. C* **2023**, *127*, 4684−4688.

(14) Byeon, P.; Bae, H. B.; Chung, H. S.; Lee, S. G.; Kim, J. G.; Lee, H. J.; Choi, J. W.; Chung, S. Y. Atomic-scale observation of $LiFePO_4$ and $LiCoO_2$ dissolution behavior in aqueous solutions. *Adv. Funct. Mater.* **2018**, *28*, 1804564.

(15) Oh, H.; Yamagishi, H.; Ohta, T.; Byon, H. R. Understanding the interfacial reactions of $LiCoO_2$ positive electrodes in aqueous lithium-ion batteries. *Mater. Chem. Front.* **2021**, *5*, 3657−3663.

(16) Motzko, M.; Carrillo Solano, M. A.; Jaegermann, W.; Hausbrand, R. Photoemission Study on the Interaction Between $LiCoO_2$ Thin Films and Adsorbed Water. *J. Phys. Chem. C* **2015**, *119*, 23407−23412.

(17) Shu, Q.; Chen, L.; Xia, Y. Y.; Gong, X. G.; Gu, X. Proton-Induced Dysfunction Mechanism of Cathodes in an Aqueous Lithium Ion Battery. *J. Phys. Chem. C* **2013**, *117*, 6929−6932.

(18) Gu, X.; Liu, J. L.; Yang, J. H.; Xiang, H. J.; Gong, X. G.; Xia, Y. Y. First-principles study of H^+ intercalation in layer-structured $LiCoO_2$. *J. Phys. Chem. C* **2011**, *115*, 12672−12676.

(19) Wang, Y.-G.; Lou, J.-Y.; Wu, W.; Wang, C.-X.; Xia, Y.-Y. Hybrid aqueous energy storage cells using activated carbon and lithium-ion intercalated compounds - III. Capacity fading mechanism of $LiCo_{1/3}Ni_{1/3}Mn_{1/3}O_2$ at different pH electrolyte solutions. *J. Electrochem. Soc.* **2007**, *154*, A228.

(20) Wang, Y.-G.; Luo, J.-Y.; Wang, C.-X.; Xia, Y.-Y. Hybrid aqueous energy storage cells using activated carbon and lithium-ion

intercalated compounds II. Comparison of $LiMn_2O_4$, $LiCo_{1/3}Ni_{1/3}Mn_{1/3}O_2$, and $LiCoO_2$ positive electrodes. *J. Electrochem. Soc.* **2006**, *153*, A1425.
(21) Cherkashinin, G.; Jaegermann, W. Dissociative adsorption of H_2O on $LiCoO_2$ (00l) surfaces: Co reduction induced by electron transfer from intrinsic defects. *J. Chem. Phys.* **2016**, *144*, 184706.
(22) Luo, J. Y.; Cui, W. J.; He, P.; Xia, Y. Y. Raising the cycling stability of aqueous lithium-ion batteries by eliminating oxygen in the electrolyte. *Nat. Chem.* **2010**, *2*, 760−765.
(23) Takamatsu, D.; Koyama, Y.; Orikasa, Y.; Mori, S.; Nakatsutsumi, T.; Hirano, T.; Tanida, H.; Arai, H.; Uchimoto, Y.; Ogumi, Z. J. A. C. I. E. First in situ observation of the $LiCoO_2$ electrode/electrolyte interface by total-reflection X-ray absorption spectroscopy. *Angew. Chem., Int. Ed.* **2012**, *51*, 11597−11601.
(24) Schulz, N.; Hausbrand, R.; Wittich, C.; Dimesso, L.; Jaegermann, W. XPS-Surface Analysis of SEI Layers on Li-Ion Cathodes: Part II. SEI-Composition and Formation inside Composite Electrodes. *J. Electrochem. Soc.* **2018**, *165*, A833−A846.
(25) Zhang, J. N.; Li, Q. H.; Wang, Y.; Zheng, J. Y.; Yu, X. Q.; Li, H. Dynamic evolution of cathode electrolyte interphase (CEI) on high voltage $LiCoO_2$ cathode and its interaction with Li anode. *Energy Storage Mater.* **2018**, *14*, 1−7.
(26) Yang, J.; Liu, H. W.; Martens, W. N.; Frost, R. L. Synthesis and Characterization of Cobalt Hydroxide, Cobalt Oxyhydroxide, and Cobalt Oxide Nanodiscs. *J. Phys. Chem. C* **2010**, *114*, 111−119.
(27) Mizokawa, T.; Wakisaka, Y.; Sudayama, T.; Iwai, C.; Miyoshi, K.; Takeuchi, J.; Wadati, H.; Hawthorn, D. G.; Regier, T. Z.; Sawatzky, G. A. Role of oxygen holes in Li_xCoO_2 revealed by soft x-ray spectroscopy. *Phys. Rev. Lett.* **2013**, *111*, 056404.
(28) Chen, C. H.; Hwang, B. J.; Chen, C. Y.; Hu, S. K.; Chen, J. M.; Sheu, H. S.; Lee, J. F. Soft X-ray absorption spectroscopy studies on the chemically delithiated commercial $LiCoO_2$ cathode material. *J. Power Sources* **2007**, *174*, 938−943.
(29) Yoon, W.-S.; Kim, K.-B.; Kim, M.-G.; Lee, M.-K.; Shin, H.-J.; Lee, J.-M.; Lee, J.-S.; Yo, C.-H. Oxygen contribution on Li-ion intercalation-deinterealation in $LiCoO_2$ investigated by O K-edge and Co L-edge X-ray absorption spectroscopy. *J. Phys. Chem. B* **2002**, *106*, 2526−2532.
(30) Liu, L.; Chen, L.; Huang, X.; Yang, X.-Q.; Yoon, W.-S.; Lee, H. S.; McBreen, J. Electrochemical and in situ synchrotron XRD studies on Al_2O_3-coated $LiCoO_2$ cathode material. *J. Electrochem. Soc.* **2004**, *151*, A1344.
(31) Menetrier, M.; Saadoune, I.; Levasseur, S.; Delmas, C. The insulator-metal transition upon lithium deintercalation from $LiCoO_2$: electronic properties and 7Li NMR study. *J. Mater. Chem.* **1999**, *9*, 1135−1140.
(32) Nakayama, M.; Ikuta, H.; Uchimoto, Y.; Wakihara, M. Study on the AC impedance spectroscopy for the Li insertion reaction of $Li_xLa_{1/3}NbO_3$ at the electrode-electrolyte interface. *J. Phys. Chem. B* **2003**, *107*, 10603−10607.
(33) Bredar, A. R. C.; Chown, A. L.; Burton, A. R.; Farnum, B. H. Electrochemical Impedance Spectroscopy of Metal Oxide Electrodes for Energy Applications. *ACS Appl. Energy Mater.* **2020**, *3*, 66−98.
(34) Lee, S. W.; Carlton, C.; Risch, M.; Surendranath, Y.; Chen, S.; Furutsuki, S.; Yamada, A.; Nocera, D. G.; Shao-Horn, Y. The Nature of Lithium Battery Materials under Oxygen Evolution Reaction Conditions. *J. Am. Chem. Soc.* **2012**, *134*, 16959−16962.
(35) Zhang, Y. J.; Cremer, P. S. Interactions between macromolecules and ions: the Hofmeister series. *Curr. Opin. Chem. Biol.* **2006**, *10*, 658−663.
(36) Reber, D.; Grissa, R.; Becker, M.; Kuhnel, R. S.; Battaglia, C. Anion Selection Criteria for Water-in-Salt Electrolytes. *Adv. Energy Mater.* **2021**, *11*, 2002913.
(37) Lim, J.; Park, K.; Lee, H.; Kim, J.; Kwak, K.; Cho, M. Nanometric Water Channels in Water-in-Salt Lithium Ion Battery Electrolyte. *J. Am. Chem. Soc.* **2018**, *140*, 15661−15667.
(38) Su, H. L.; Lan, M. T.; Lin, K. W.; Hsieh, Y. Z. J. E. Chaotropic salts: Novel modifiers for the capillary electrophoretic analysis of benzodiazepines. *Electrophoresis* **2008**, *29*, 3384−3390.
(39) O'Brien, J. T.; Prell, J. S.; Bush, M. F.; Williams, E. R. Sulfate Ion Patterns Water at Long Distance. *J. Am. Chem. Soc.* **2010**, *132*, 8248−8249.
(40) Omta, A. W.; Kropman, M. F.; Woutersen, S.; Bakker, H. J. Negligible effect of ions on the hydrogen-bond structure in liquid water. *Science* **2003**, *301*, 347−349.
(41) Schwierz, N.; Horinek, D.; Sivan, U.; Netz, R. R. Reversed Hofmeister series-The rule rather than the exception. *Curr. Opin. Colloid Interface Sci.* **2016**, *23*, 10−18.
(42) Dubouis, N.; Lemaire, P.; Mirvaux, B.; Salager, E.; Deschamps, M.; Grimaud, A. The role of the hydrogen evolution reaction in the solid-electrolyte interphase formation mechanism for "Water-in-Salt" electrolytes. *Energy Environ. Sci.* **2018**, *11*, 3491−3499.
(43) Lee, M. H.; Kim, S. J.; Chang, D.; Kim, J.; Moon, S.; Oh, K.; Park, K. Y.; Seong, W. M.; Park, H.; Kwon, G.; et al. Toward a low-cost high-voltage sodium aqueous rechargeable battery. *Mater. Today* **2019**, *29*, 26−36.
(44) Cammarata, L.; Kazarian, S. G.; Salter, P. A.; Welton, T. Molecular states of water in room temperature ionic liquids. *Phys. Chem. Chem. Phys.* **2001**, *3*, 5192−5200.
(45) Liu, J. H.; Zhang, Y. H.; Wang, L. Y.; Wei, Z. F. Drawing out the structural information of the first layer of hydrated ions: ATR-FTIR spectroscopic studies on aqueous NH_4NO_3, $NaNO_3$, and $Mg(NO_3)_2$ solutions. *Spectrochim. Acta, Part A* **2005**, *61*, 893−899.
(46) Kitadai, N.; Sawai, T.; Tonoue, R.; Nakashima, S.; Katsura, M.; Fukushi, K. Effects of ions on the OH stretching band of water as revealed by ATR-IR spectroscopy. *J. Solution Chem.* **2014**, *43*, 1055−1077.
(47) Cheng, F. Q.; Cao, Q. B.; Guan, Y. S.; Cheng, H. G.; Wang, X. M.; Miller, J. D. FTIR analysis of water structure and its influence on the flotation of arcanite (K_2SO_4) and epsomite ($MgSO_4{\cdot}7H_2O$). *Int. J. Miner. Process.* **2013**, *122*, 36−42.
(48) Wei, Z. F.; Zhang, Y. H.; Zhao, L. J.; Liu, J. H.; Li, X. H. Observation of the first hydration layer of isolated cations and anions through the FTIR-ATR difference spectra. *J. Phys. Chem. A* **2005**, *109*, 1337−1342.
(49) Chen, Y.; Zhang, Y. H.; Zhao, L. J. ATR-FTIR spectroscopic studies on aqueous $LiClO_4$, $NaClO_4$, and $Mg(ClO_4)_2$ solutions. *Phys. Chem. Chem. Phys.* **2004**, *6*, 537−542.
(50) Rull, F.; Ohtaki, H. Raman spectral studies on ionic interaction in aqueous alkali sulfate solutions. *Spectrochim. Acta, Part A* **1997**, *53*, 643−653.
(51) Rull, F. Raman-spectroscopic study of the ion association of lithium-sulfate aqueous-solutions. *Zeitschrift Fur Naturforschung Section a-a Journal of Physical Sciences* **1995**, *50*, 292−300.
(52) Yu, J. Y.; Zhang, Y.; Tan, S. H.; Liu, Y.; Zhang, Y. H. Observation on the Ion Association Equilibria in $NaNO_3$ Droplets Using Micro-Raman Spectroscopy. *J. Phys. Chem. B* **2012**, *116*, 12581−12589.
(53) Miller, A. G.; Macklin, J. W. Vibrational spectroscopic studies of sodium-perchlorate contact ion-pair formation in aqueous-solution. *J. Phys. Chem.* **1985**, *89*, 1193−1201.
(54) Bhattacharjee, S.; Khan, S. The wetting behavior of aqueous imidazolium based ionic liquids: a molecular dynamics study. *Phys. Chem. Chem. Phys.* **2020**, *22*, 8595−8605.
(55) Gorska, B.; Timperman, L.; Anouti, M.; Beguin, F. Effect of low water content in protic ionic liquid on ions electrosorption in porous carbon: application to electrochemical capacitors. *Phys. Chem. Chem. Phys.* **2017**, *19*, 11173−11186.
(56) Chiang, C. H.; Chen, C. C.; Nazeeruddin, M. K.; Wu, C. G. A newly developed lithium cobalt oxide super hydrophilic film for large area, thermally stable and highly efficient inverted perovskite solar cells. *J. Mater. Chem. A* **2018**, *6*, 13751−13760.
(57) Lim, H. K.; Lee, H.; Kim, H. A Seamless Grid-Based Interface for Mean-Field QM/MM Coupled with Efficient Solvation Free Energy Calculations. *J. Chem. Theory Comput.* **2016**, *12*, 5088−5099.
(58) Motobayashi, K.; Shibamura, Y.; Ikeda, K. J. E. C. Potential-induced interfacial restructuring of a pyrrolidinium-based ionic liquid

https://doi.org/10.1021/jacsau.3c00061
JACS Au 2023, 3, 1392−1402

on an Au electrode: Effect of polarization of constituent ions. *Electrochem. Commun.* **2019**, *100*, 117−120.
(59) Peak, D.; Ford, R. G.; Sparks, D. L. An in situ ATR-FTIR investigation of sulfate bonding mechanisms on goethite. *J. Colloid Interface Sci.* **1999**, *218*, 289−299.
(60) McQuillan, A. J.; Osawa, M.; Peak, D.; Ren, B.; Tian, Z. Q. Experiments on adsorption at hydrous metal oxide surfaces using attenuated total reflection infrared spectroscopy (ATRIRS) (IUPAC Technical Report). *Pure Appl. Chem.* **2019**, *91*, 2043−2061.
(61) Hoshino, S.; Glushenkov, A. M.; Ichikawa, S.; Ozaki, T.; Inamasu, T.; Yabuuchi, N. Reversible three-electron redox reaction of Mo^{3+}/Mo^{6+} for rechargeable lithium batteries. *ACS Energy Lett.* **2017**, *2*, 733−738.
(62) Yun, J.; Sagehashi, R.; Sato, Y.; Masuda, T.; Hoshino, S.; Rajendra, H. B.; Okuno, K.; Hosoe, A.; Bandarenka, A. S.; Yabuuchi, N. Nanosized and metastable molybdenum oxides as negative electrode materials for durable high-energy aqueous Li-ion batteries. *Proc. Natl. Acad. Sci. U.S.A.* **2021**, *118*, 7.
(63) Lukomska, A.; Sobkowski, J. Potential of zero charge of monocrystalline copper electrodes in perchlorate solutions. *J. Electroanal. Chem.* **2004**, *567*, 95−102.
(64) Finke, C. E.; Omelchenko, S. T.; Jasper, J. T.; Lichterman, M. F.; Read, C. G.; Lewis, N. S.; Hoffmann, M. R. Enhancing the activity of oxygen-evolution and chlorine-evolution electrocatalysts by atomic layer deposition of TiO_2. *Energy Environ. Sci.* **2019**, *12*, 358−365.
(65) Giannozzi, P.; Baroni, S.; Bonini, N.; Calandra, M.; Car, R.; Cavazzoni, C.; Ceresoli, D.; Chiarotti, G. L.; Cococcioni, M.; Dabo, I.; et al. QUANTUM ESPRESSO: a modular and open-source software project for quantum simulations of materials. *J. Phys. Condens. Matter* **2009**, *21*, 395502.
(66) Plimpton, S. Fast parallel algorithms for short-range molecular-dynamics. *J. Comput. Phys.* **1995**, *117*, 1−19.
(67) Gim, S.; Lim, H. K.; Kim, H. Multiscale Simulation Method for Quantitative Prediction of Surface Wettability at the Atomistic Level. *J. Phys. Chem. Lett.* **2018**, *9*, 1750−1758.
(68) Gim, S.; Cho, K. J.; Lim, H. K.; Kim, H. Structure, Dynamics, and Wettability of Water at Metal Interfaces. *Sci. Rep.* **2019**, *9*, 14805.
(69) Cho, K. J.; Gim, S.; Lim, H. K.; Kim, C.; Kim, H. Water Slippage on Graphitic and Metallic Surfaces: Impact of the Surface Packing Structure and Electron Density Tail. *J. Phys. Chem. C* **2020**, *124*, 11392−11400.
(70) Abbaspour-Tamijani, A.; Bennett, J. W.; Jones, D. T.; Cartagena-Gonzalez, N.; Jones, Z. R.; Laudadio, E. D.; Hamers, R. J.; Santana, J. A.; Mason, S. E. DFT and thermodynamics calculations of surface cation release in $LiCoO_2$. *Appl. Surf. Sci.* **2020**, *515*, 145865.
(71) Blochl, P. E. Projector augmented-wave method. *Phys. Rev. B* **1994**, *50*, 17953−17979.
(72) Perdew, J. P.; Burke, K.; Ernzerhof, M. Generalized gradient approximation made simple. *Phys. Rev. Lett.* **1996**, *77*, 3865−3868.
(73) Zhou, F.; Cococcioni, M.; Marianetti, C. A.; Morgan, D.; Ceder, G. First-principles prediction of redox potentials in transition-metal compounds with LDA + U. *Phys. Rev. B* **2004**, *70*, 235121.
(74) Price, D. J.; Brooks, C. L. A modified TIP3P water potential for simulation with Ewald summation. *J. Chem. Phys.* **2004**, *121*, 10096−10103.
(75) Jeon, J.; Kim, H.; Goddard, W. A.; Pascal, T. A.; Lee, G. I.; Kang, J. K. The Role of Confined Water in Ionic Liquid Electrolytes for Dye-Sensitized Solar Cells. *J. Phys. Chem. Lett.* **2012**, *3*, 556−559.
(76) Pegado, L.; Marsalek, O.; Jungwirth, P.; Wernersson, E. Solvation and ion-pairing properties of the aqueous sulfate anion: explicit versus effective electronic polarization. *Phys. Chem. Chem. Phys.* **2012**, *14*, 10248−10257.
(77) Joung, I. S.; Cheatham, T. E. Determination of alkali and halide monovalent ion parameters for use in explicitly solvated biomolecular simulations. *J. Phys. Chem. B* **2008**, *112*, 9020−9041.
(78) Liu, X. M.; Zhang, S. J.; Zhou, G. H.; Wu, G. W.; Yuan, X. L.; Yao, X. Q. New force field for molecular simulation of guanidinium-based ionic liquids. *J. Phys. Chem. B* **2006**, *110*, 12062−12071.
(79) Thogersen, J.; Rehault, J.; Odelius, M.; Ogden, T.; Jena, N. K.; Jensen, S. J. K.; Keiding, S. R.; Helbing, J. Hydration Dynamics of Aqueous Nitrate. *J. Phys. Chem. B* **2013**, *117*, 3376−3388.
(80) Rappe, A. K.; Casewit, C. J.; Colwell, K. S.; Goddard, W. A.; Skiff, W. M. UFF, a full periodic table force field for molecular mechanics and molecular dynamics simulations. *J. Am. Chem. Soc.* **1992**, *114*, 10024−10035.
(81) Nose, S. A unified formulation of the constant temperature molecular dynamics methods. *J. Chem. Phys.* **1984**, *81*, 511−519.
(82) Hoover, W. G. Canonical dynamics: Equilibrium phase-space distributions. *Phys. Rev. A* **1985**, *31*, 1695−1697.

https://doi.org/10.1021/jacsau.3c00061
JACS Au 2023, 3, 1392−1402